

RESEARCH

Open Access



Effect of Fiber Orientation on the Fatigue Behavior of Steel Fiber-Reinforced Concrete Specimens by Performing Wedge Splitting Tests and Computed Tomography Scanning

Dorys C. González^{1*} , Álvaro Mena-Alonso¹, Jesús Mínguez¹, José A. Martínez¹ and Miguel A. Vicente¹

Abstract

This paper shows the relationship, in steel fiber-reinforced concrete, between fiber orientation and fatigue response through the combined use of computed tomography (CT), digital image processing (DIP) software and wedge splitting test (WST). The WST cubes were extracted from conventional 150 × 150 × 600 concrete prisms and a groove and notch were carved on different faces in such a way that in half of the test specimens the fibers are oriented mostly perpendicular to the breaking surface and, in the other half, the fibers are mostly oriented parallel to the breaking surface. Fiber orientation was obtained using a CT device and DIP software from a miniprism extracted from the previously mentioned concrete prisms. The results show that there is a strong correlation between the crack-sewing fiber orientation on the one hand and fatigue life and crack opening rate per cycle on the other hand. Cubes with a higher percentage of fibers perpendicular to the crack surface (i.e., with a higher efficiency index) show a longer fatigue life and a lower crack opening rate per cycle, while cubes with a lower efficiency index show a shorter fatigue life and a higher crack opening rate per cycle.

Keywords Fiber-reinforced concrete, CT-scan technology, Crack patterns, Wedge splitting test, Fatigue creep curve

1 Introduction

Fiber-reinforced concrete is a technical solution of great interest in civil engineering due to the numerous advantages it offers over traditional structural concrete solutions. The fields of application of this building material are multiple, covering almost all structural elements traditionally built with reinforced concrete, as well as other new applications. Moreover, nowadays, due to the growing concern about the environmental impact of civil

constructions, interest in fiber-reinforced concrete has increased and quite a few promising research projects are being carried out using natural fibers (Ahmand & Zhou, 2022; Khan et al., 2020; Shah et al., 2022).

One of the most common uses of fibers is to reduce concrete cracking, caused by shrinkage and thermal variations, among others. Therefore, fibers improve the durability of concrete (Nogueira et al., 2021; Saradar et al., 2018; Shen et al., 2022; Vrijdaghs et al., 2018; Zia & Ali, 2017). This application is particularly suitable for elements that do not require rebar structural reinforcement. In these situations, the minimum reinforcement ratios specified in the standards can be easily covered with normal fiber contents.

However, the greatest research efforts are being made in the field of the use of fibers as a structural component to replace the traditional rebar reinforcement totally or

Journal information: ISSN 1976-0485 / eISSN 2234-1315.

*Correspondence:

Dorys C. González
dgonzalez@ubu.es

¹ E. Politécnica Superior, Universidad de Burgos, Campus Milanera (Edif. D), c/Villadiego s/n, 09001 Burgos, Spain



© The Author(s) 2023. **Open Access** This article is licensed under a Creative Commons Attribution 4.0 International License, which permits use, sharing, adaptation, distribution and reproduction in any medium or format, as long as you give appropriate credit to the original author(s) and the source, provide a link to the Creative Commons licence, and indicate if changes were made. The images or other third party material in this article are included in the article's Creative Commons licence, unless indicated otherwise in a credit line to the material. If material is not included in the article's Creative Commons licence and your intended use is not permitted by statutory regulation or exceeds the permitted use, you will need to obtain permission directly from the copyright holder. To view a copy of this licence, visit <http://creativecommons.org/licenses/by/4.0/>.

partially (Gao et al., 2021; Lee, 2017; Mobasher et al., 2014; Mudadu et al., 2018; Nilforoush et al., 2017; Ortega et al., 2022; Yoo & Yoon, 2015; Yuan & Jian, 2021). At this point, fiber-reinforced concrete is a very competitive option in civil engineering works, since it represents a significant cost saving, especially in labor, compared to conventional reinforced concrete. However, its implementation remains a technical challenge that has not yet been fully solved.

Among the different mechanical solicitations to which a fiber-reinforced concrete element may be subjected, fatigue is the one that currently arouses most scientific interest. There are two major structural elements where fatigue is the most important loading condition: concrete pavements and wind turbine structures (mainly foundations and towers). In both cases, the use of fiber-reinforced concrete (instead of conventional reinforced concrete) has great technological interest (Ali et al., 2020a, 2020b; Batrukin et al., 2021; Cui et al., 2023; González et al., 2014; Ozturk & Ozyurt, 2022; Yazdanbakhsh et al., 2018).

In addition to the fiber content, the orientation of the fibers within the concrete matrix is an aspect that largely conditions the macroscopic response of the elements. However, its study is not straightforward, since the fiber arrangement is in principle random and cannot be easily controlled. It strongly depends on the size and shape of the specimens (due to the wall effect), the manufacturing process (whether the specimen is molded, drilled or cut) and the length of the fibers, among other aspects (Conforti et al., 2021; Laranjeira et al., 2011; Riedel & Leutbecher, 2021; Vicente et al., 2019a; Zhou & Uchida, 2017). In most of the published investigations, specimens showing uniform, preferred fiber orientations are usually tested.

The technical literature contains some interesting works in which series of specimens with clearly different fiber orientations have been fabricated. In this sense, it is worth mentioning the work carried out by Mínguez and collaborators (Mínguez et al., 2018). In this paper, a small concrete wall was built from which concrete prisms were extracted according to different orientations and positions. These prisms were subjected to 3-point bending tests to evaluate the flexural strength. It was expected (as it finally happened), that the fibers would be aligned in the horizontal plane and substantially parallel to the main direction of the wall. Therefore, the prisms extracted in the horizontal direction showed fibers oriented mainly orthogonal to the failure surface, while in the prisms extracted in the vertical direction, the fibers were mainly oriented parallel to it. In addition, the fibers (steel fibers were used) tended to be located towards the bottom of the wall, so the percentage of fibers was higher in the

prisms extracted from the bottom of the wall than in those from the top.

Similarly, the paper of Gonzalez and coworkers (González et al., 2018a) is noteworthy. In it, fiber-reinforced concrete prisms were fabricated from which cubes were extracted and then subjected to wedge splitting tests (WST) in two different configurations. In this case, it was expected that the fibers would be oriented in the horizontal plane, so that in one series of cubes the fibers would be arranged perpendicular to the cracking surface, while in another series the fibers would be mainly parallel to it.

However, in these two works fatigue tests were not performed, but static ones. In general, research focusing on the effect of fiber orientation on the fatigue response of concrete is scarce, being more common in compressive fatigue (Cachim et al., 2002; Cui et al., 2021; Khan et al., 2022; Medeiros et al., 2015; Mínguez et al., 2019) than in tensile (Deng et al., 2021; Isojeh et al., 2017; Martinello et al., 2019; Vicente et al., 2019b).

The main issue in any study of the influence of fiber orientation on the macroscopic behavior of fiber-reinforced concrete is to determine the real orientation of the fibers within the specimens. There are techniques that provide average values of fiber orientations based on indirect parameters such as inductivity (Al-Mattarneh, 2014; Li et al., 2020) or permittivity (Akgol et al., 2019; Mehdi-pour et al., 2017). These methods are fast, relatively inexpensive and can be used on site. However, their main drawback is their lack of accuracy.

X-ray micro-computed tomography is the technology that provides the most accurate results of the position, distribution and orientation of fibers in concrete. It requires expensive scientific equipment, but the results are of high quality and offer unlimited possibilities for research. In an X-ray tomography, a three-dimensional image of the sample is obtained, in which all the fibers inside the concrete are perfectly identified.

For this reason, in recent years it has become established as the reference technique for assessing the geometric and morphological parameters of fibers within the concrete matrix (Balazs et al., 2017; González et al., 2020; Herrmann et al., 2016; Oesch et al., 2018; Pastorelli & Herrmann, 2016; Ponikiewski & Katzer, 2016; Ríos et al., 2020; Ruan & Poursaee, 2019; Vicente et al., 2018). Among its many advantages, some of which have already been mentioned, is that of being a non-destructive method (Mena et al. 2020; Vicente et al., 2014, 2017, 2019, 2021).

The research presented here is a continuation of González et al., 2018a. The fatigue wedge splitting tests performed here have the same setup as the static ones described in the previous work.

In this study, a fiber-reinforced concrete mixture was evaluated. Eight prisms of 150×150×600 mm were fabricated. Two 150-mm side cubes were extracted from each prism. The cubes were cut so that the fibers of each cube had a significantly different orientation. The orientation of the fibers of each prism was obtained by micro-computed tomography. Finally, the results were compared and analyzed.

This paper is structured as follows: The experimental procedure is presented in Sect. 2, the results of the tests are described and discussed in Sect. 3; and finally the conclusions are found in Sect. 4.

2 Experimental Program

The materials, the manufacturing procedure and the scanning procedure are described in this section.

2.1 Materials

Eight prisms 150×150×600 mm were cast to perform this work. Table 1 shows the mix proportion.

The Portland cement used was CEM I 52.5 R. A 2% in volume of steel fibers Dramix 3D 55/60 BG (BEKAERT, Kortrijk, Belgium), 60 mm in length and 1.05 mm in thickness were used. Additionally, superplasticizer

MasterGlenium 51 (BASF, Ludwigshafen, Germany) and nano-silica MasterRoc MS 685 (BASF, Ludwigshafen, Germany) were used. Tap water has been used (Forsat et al., 2019; Shahrabadi et al., 2017).

In addition, three cylinders 150 mm in diameter and 300 mm in height were performed and tested under compression to characterize their compression strength [according to EN 196–1:2016 (British Standards Institution, 2016)]. The specimens were cured in a humid chamber (20°C and 100% humidity) for 28 days. They were then cured outside the humid chamber, in the laboratory, until the time of testing. The tests started when the specimens were 4 years old. At the beginning to the testing campaign, the average concrete compressive strength was 86.9 MPa with a standard deviation of 2.7 MPa.

2.2 Specimen Manufacturing Process

Eight couples of cubes (i.e., sixteen cubes) 150 mm in edge were extracted from the eight 150×150×600 mm prisms. Two cubes were obtained from each prism, located approximately at 1/3 and 2/3 of the lateral side of the prism (Fig. 1). Additionally, eight miniprims were extracted from the center of each prism for the CT scanning.

A groove and a notch were then carved in each cube (Fig. 2). On one of the couple's cubes, the groove and the notch were performed on the top face along the transverse axis of the prism. On the other couple's cubes, the groove and the notch were cut on the side face closest to the center of the prisms and, again, along the transverse axis of the prism. The first set of cubes is called "top" while the second one is called "side". Finally, a total of eight top cubes and eight side cubes were performed.

It is expected that the fibers are mainly oriented parallel to the longest side of the prism. This means that, in the case of the top cubes, fibers are expected to be

Table 1 Mix proportion

Materials (kg/m ³)	Mix proportion
Cement	400
Fine aggregate	800
Coarse aggregate	1080
Nanosilica	6
Water	125
Superplasticizer	14
Steel fibers	150

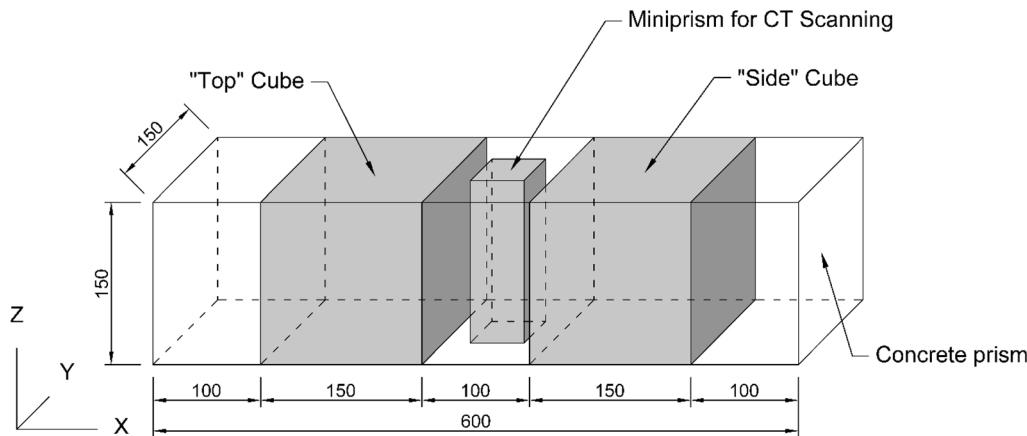


Fig. 1 Scheme of the extraction of the cubes and the miniprism

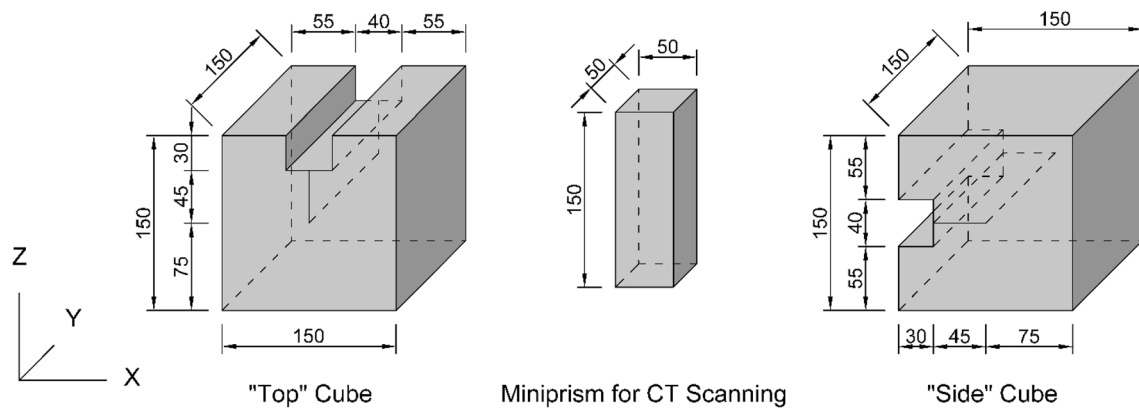


Fig. 2 Geometry of the cubes and the miniprism

oriented perpendicular to the notch and, finally, to the crack, while in the case of the side cubes, fibers are expected to be mainly oriented parallel to the notch and the crack. This forces the fibers to have clearly different orientations with respect to the plane of the crack.

In addition, a prismatic piece was cut from the center of each prism (Figs. 1 and 2). This piece as a squared section 0 mm side and a length of 150 mm. Because of the limitation of the CT-Scan device, these specimens were scanned to obtain the fibers orientation, instead of the whole prisms. Consequently, it is assumed that this miniprism is representative of the complete prism and, consequently, of the two cubes extracted from it (in terms of fiber orientation).

2.3 Scanning Process

The small prisms mentioned above were scanned using a MicroCT Phoenix V|Tome|X s 240 unit from GE

Sensing & Inspections Technologies (Boston, MA, USA), equipped with a high-power nanofocus X-ray tube (180 kV/20 W) and a high-power microfocus tube (240 kV/320 W). A total of 4,300 2D slices (Fig. 3) were obtained throughout the height of the miniprism. The voxel size is $35 \times 35 \times 35 \mu\text{m}^3$. Using the post-processing software package, a 3D image of the specimens was created. A gray level was assigned to each voxel of this three-dimensional object depending on the real density of the matter at that point. Since 16-bit images are used, the gray scale varied from 0 to 65,535, where 0 means pure black, which is least dense (corresponding to pores) and 65,535 means pure white, which is densest (corresponding to steel fibers). The result of this first post-process was a file including the X, Y and Z coordinates of the center of each voxel and its gray level. The total number of voxels in each miniprism was approximately $9.1 \cdot 10^9$.

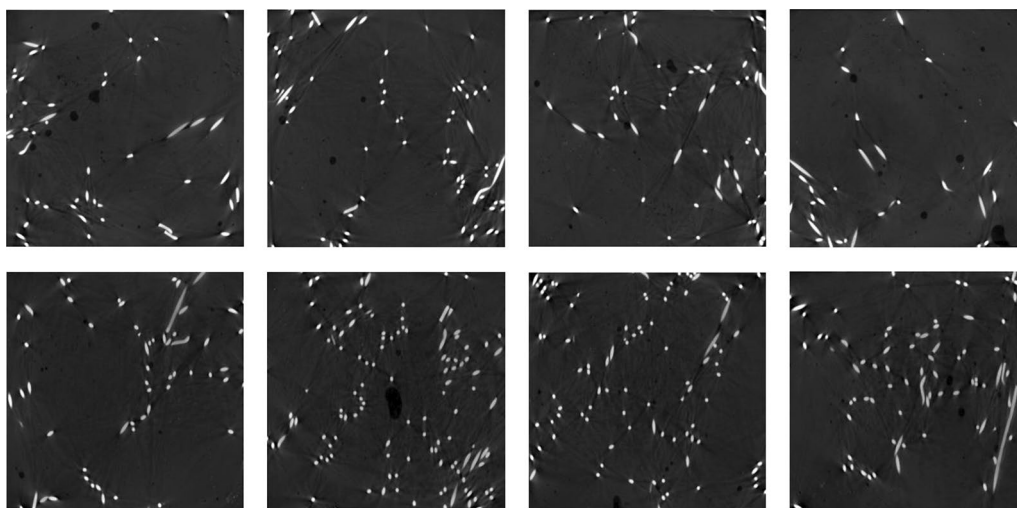


Fig. 3 Example of some slices binarized belonging to a miniprims

The information of the files mentioned above was next post-processed using the commercial software AVIZO (FEI Visualization Sciences Group, Hillsboro, OR, USA). This tool identifies and isolates each individual fiber inside the prism. The first step consists on extracting all the voxels belonging to the fibers, which were defined on the basis of a certain gray level. In this case, a lower gray threshold of 30,000 was considered appropriate. Therefore, all voxels whose gray level was between 27,000 and 65,535 were considered as fibers. As a general criterion, the gray threshold is taken in a valley of the gray distribution histogram, since the valleys correspond to the boundaries between the different components of the material (Fig. 4).

Next, all the voxels in contact were added, since they belonged to the same fiber. Subsequently, the software proceeded to separate all those fibers that had been joined by small necks. In these cases, the voxel aggregation subroutine resulted in one fiber when in fact there are two or more fibers very close to each other. An algorithm based on watershed segmentation (Vicente et al., 2021) was applied. The final result of this image analysis is a new file containing the X, Y and Z coordinates of the center of each fiber, its length (as the largest Feret's diameter) and the orientation of the axis containing the length. The orientations is provided in Cartesian coordinates, i.e., the direction angles of the axis are given. Fig. 5 shows the 3D images of two of the six miniprisms.

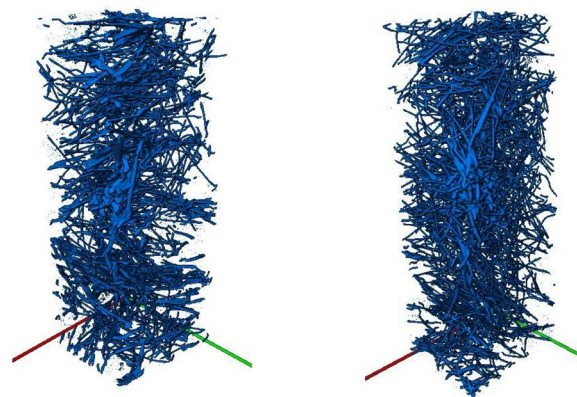


Fig. 5 Examples of 3D view of the fibers' distribution in two miniprisms

Fig. 5 shows how the fiber orientation is clearly different in two miniprisms extracted from two apparently identical prisms. The specimen on the left shows a lower fiber density. On the other hand, in the specimen on the right, the fiber density is clearly higher. Both miniprisms show different fiber orientation patterns.

In this work, fibers with a length less than 2 mm were discarded as too small. These are ends or fibers, cut during the extraction process.

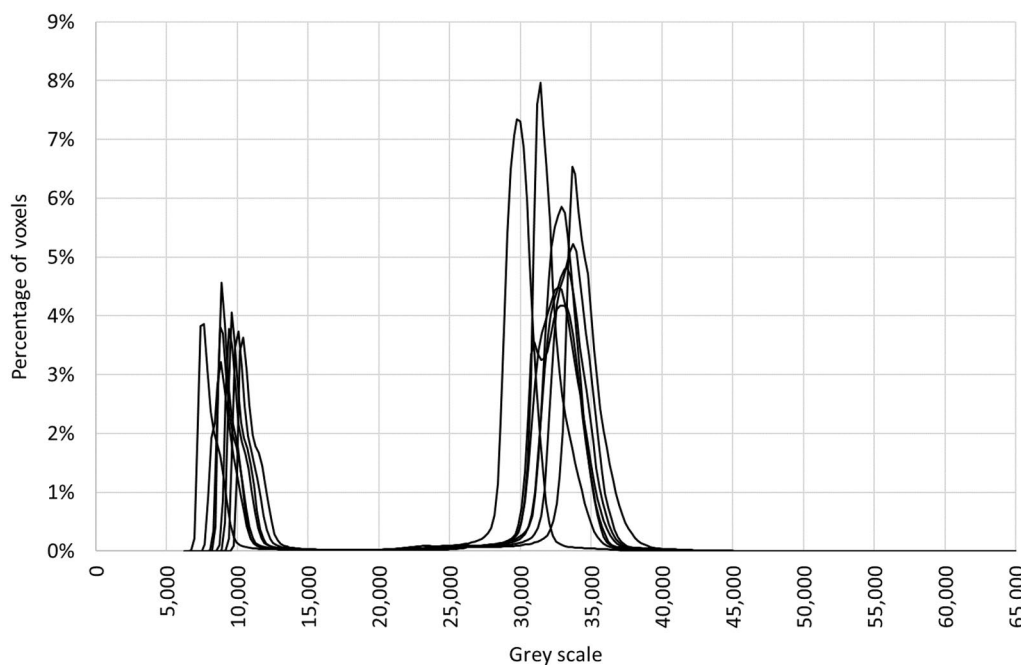


Fig. 4 Histograms of grey distribution

2.4 Wedge Splitting Test

The traditional test to measure the mechanical behavior of concrete under tension is the 3-point bending test (3PBT), which can be carried out according the standards EN 14651:2005+A1:2007 (British Standards Institution, 2008) or ASTM C1609 (American Society for Testing & Materials, 2019), among others. One of the main limitations of this test is that the fibers tend to show a preferential orientation, due to the boundary conditions of the mold, the concreting direction, etc., which directly affect the results.

An alternative test to the 3PBT is the wedge splitting test (WST). This test was first proposed and described by Linsbauer and Tschegg (Linsbauer & Tschegg, 1986) and next developed by Brühwiler and Wittmann (Brühwiler & Wittmann, 1990). In this research, it is used to evaluate the fatigue life of fiber-reinforced concrete in tension.

Once the cubes had been extracted from the prism, they were prepared by sawing a groove and a notch (Fig. 6). As explained before, a novelty of this research is that the groove and the notch were sawed in two different faces, belonging to two different orientation. In consequence, it is expected that the orientation of the fibers is clearly different in the cubes belonging to the different series.

The cubes were placed on a square steel bar 20 mm in width, centered in the specimen and parallel to the groove's direction. Two steel L-shape devices equipped with two rollers each were placed on the top of the specimen at the both lips of the groove. In addition, a

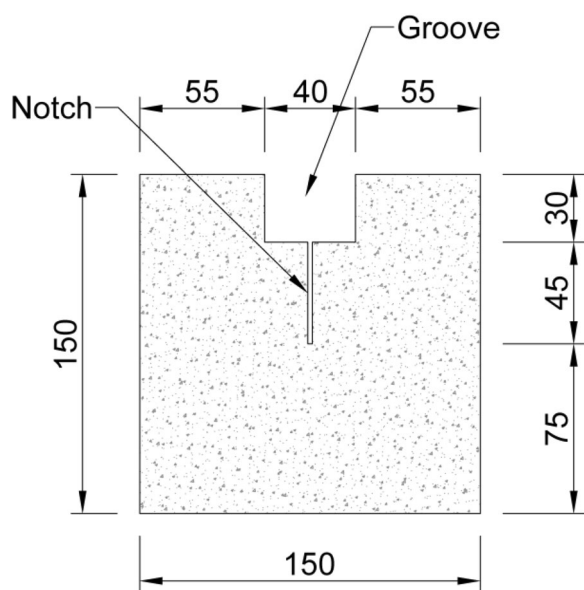


Fig. 6 Dimensions of the groove and the notch

steel U-shape piece made up of two steel wedges were hanged from the hydraulic cylinder (Fig. 7).

During the test, the following parameters were measured: the applied load and the crack mouth opening displacement (CMOD). A tension–compression MTS 244.21 dynamic hydraulic cylinder (MTS, Eden Prairie, MN) was used, with a capacity of ± 50 kN. The actuator had a load cell MTS 661.20 F-02 (MTS, Eden Prairie, MN), with a range of ± 50 kN too and an error of below 1% of the range. For the measure of the CMOD, four laser distance sensor WENGLOR CP08MHT80 (WENGLOR, Tettngang, Germany) were used with a range of 50 mm and an accuracy of 0.01 mm. For the measure of the crack opening displacement, one MTS 624.12 F-24 clip gauge (MTS, Eden Prairie, MN) was used with a range of 15 mm and an accuracy of 0.01 mm.

The laser distance sensors were placed at the bottom of the notch, i.e., at the beginning of the crack to measure accurately the CMOD while the clip gauge was placed at the beginning of the notch, centered on the concrete cube (Fig. 7).

Two of the laser distance sensors were placed on the front face and the other two were placed on the rear face. The body of the sensor remained fixed and it monitor the distance to a L-shaped small piece glued to the specimen close to the end of the notch, i.e., at the beginning of the crack. The crack opening at a face was obtained as the sum of the displacement measured by the two laser distance sensors. Finally, the crack width, or CMOD, is defined as the average value of the measures of the crack openings of the front and rear faces. The measurement provided by the clip gauge was used as a contrast, to verify that the data provided by the laser distance sensors were consistent.

The test campaign had two stages. In the first stage, all the specimens were subjected to a static test until

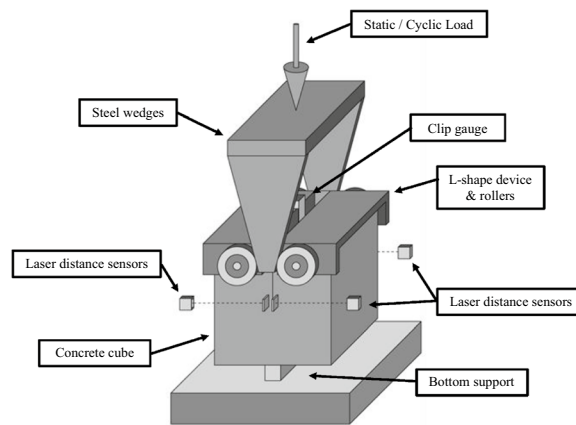


Fig. 7 Scheme of the WST. General view

the crack appeared. During this test, an increasing vertical load F_V was applied. The test was displacement-controlled and the tension speed was 0.05 mm/min until the maximum load is reached. The test stopped when the load decreased below 95% of the maximum vertical load or the CMOD reached a value of 0.5 mm (the condition that was first fulfilled).

At the end of this first stage of the test campaign, all the test specimens are pre-cracked. Then, in a second stage of the test campaign, the specimens were subjected to cyclic loading between 85 and 5% of the maximum load, measured in the pre-cracking test described above. The testing frequency was 5 Hz and the data recording frequency was 50 Hz.

In the wedge splitting test, the vertical force is decomposed, at the roller level in two forces, a vertical force $0.5 \cdot F_V$ and a horizontal force F_H , according to the following expression (Eq. 1):

$$F_H = \frac{F_V}{2 \cdot \operatorname{tg}(\alpha)}, \tag{1}$$

where α is the wedge angle. In this case, $\alpha = 15^\circ$.

According to the Strength of Materials, both vertical and horizontal force cause a tension force and a bending moment at the collapse cross-section, according to the following expressions (Eq. 2):

$$N = \frac{F}{2 \cdot \operatorname{tg}(\alpha)}, \tag{2}$$

$$M = \frac{F}{2 \cdot \operatorname{tg}(\alpha)} \cdot \left(b + \frac{h}{2}\right) + \frac{F}{4} \cdot a.$$

The tension stress σ can then be obtained considering a linear-elastic behavior of the material (Eq. 3).

$$\sigma = \frac{N}{A} + \frac{M}{W} = \frac{N}{b \cdot h} + \frac{6 \cdot M}{b \cdot h^2} \tag{3}$$

In this case, $a = 76\text{mm}$, $b = 60\text{mm}$ and $h = 75\text{mm}$ (Fig. 8).

3 Results and Discussion

Several correlations between the fiber orientation and the fatigue behavior of fiber-reinforced concrete under tension can be obtained using the information provided by the CT-Scan and the one obtained through the wedge splitting test.

3.1 Fiber Orientation

The CT-Scan and the DIP software provide the necessary information to obtain the fiber orientation with respect to each of the Cartesian axes X, Y and Z (see Fig. 2), i.e., the direction angles of the length axis of the fiber. Next, the

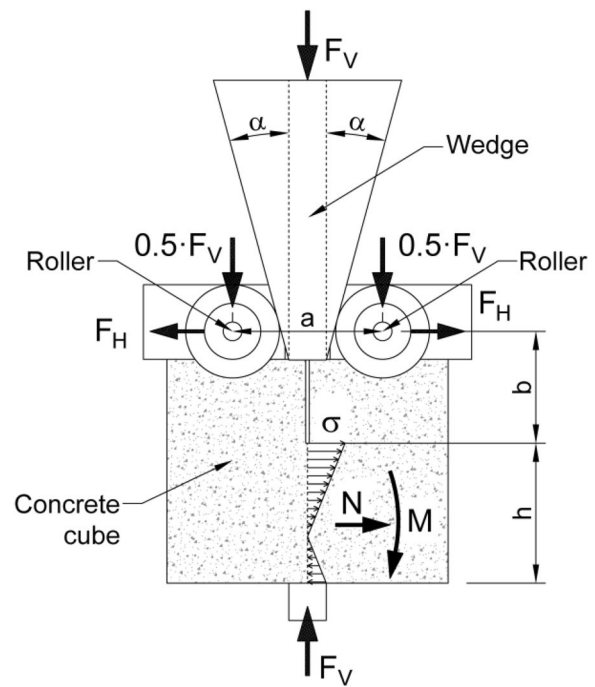


Fig. 8 Mechanical behavior of the WST

histograms of angle distribution are shown for each mini-prism (Figs. 9, 10, 11).

Figs. 9, 10, 11 reveal that fibers are substantially oriented along the XY plane, i.e., perpendicularly to the Z-axis. This is the expected result, since the process of filling the prisms and the vibration of the molds means that the fibers tend to be arranged horizontally. With respect to the X and Y axes it is not observed a dominant orientation, i.e., fibers are uniformly distributed in the XY plane. It should be noted that, in the X and Y directions, some specimens show a slightly different behavior than the rest, presumably of a random nature.

Using the data shown in Figs. 9, 10, 11, it is possible to obtain a parameter called efficiency index with respect to the X, Y and Z axes, respectively (ei_x , ei_y and ei_z), according to the following equations (Eq. 4) (González et al., 2018a; Mínguez et al., 2018; Vicente et al., 2019a):

$$\begin{aligned} ei_x &= \sum_{i=1}^n f_{i,x} \cdot \cos(\bar{\alpha}_x), \\ ei_y &= \sum_{i=1}^n f_{i,y} \cdot \cos(\bar{\alpha}_y), \\ ei_z &= \sum_{i=1}^n f_{i,z} \cdot \cos(\bar{\alpha}_z), \end{aligned} \tag{4}$$

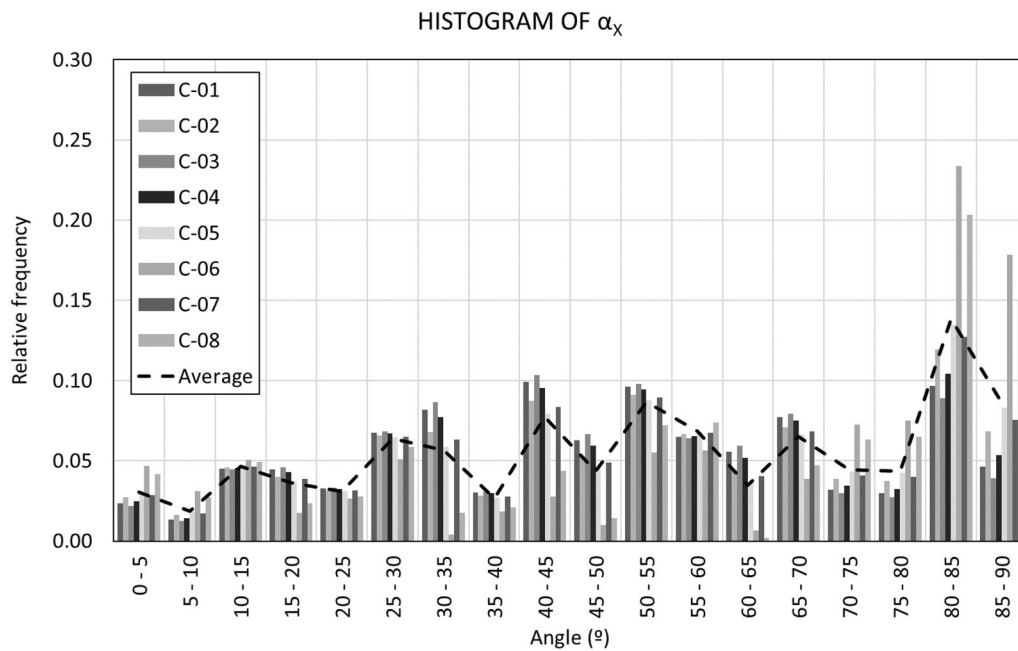


Fig. 9 Histogram of angle distribution with respect to the X-axis

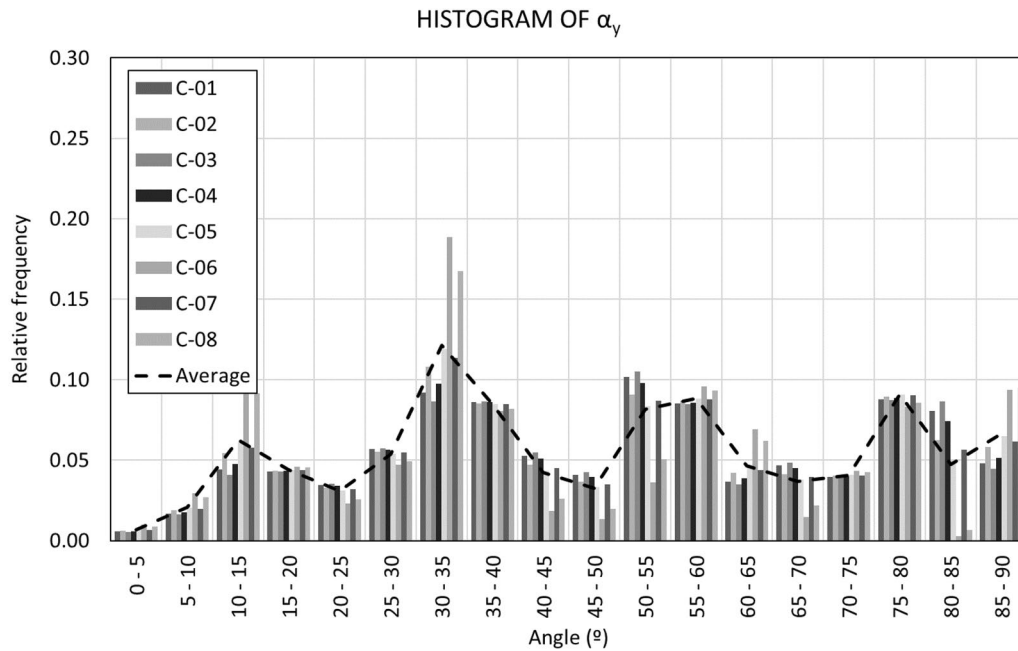


Fig. 10 Histogram of angle distribution with respect to the Y-axis

where $f_{i,x}$, $f_{i,y}$ and $f_{i,z}$ are the relative frequencies of the fiber orientation with respect to the X, Y and Z axes, respectively, $\bar{\alpha}_x$, $\bar{\alpha}_y$ and $\bar{\alpha}_z$ the average angle of each range and n the number of ranges in which the histogram is divided (18 in this case).

The efficiency index may vary between 0 and 1, where 0 means that all the fibers are perpendicular to that axis and 1 means that all the fibers are aligned to that axis.

Table 2 shows the efficiency index values for all the prisms.

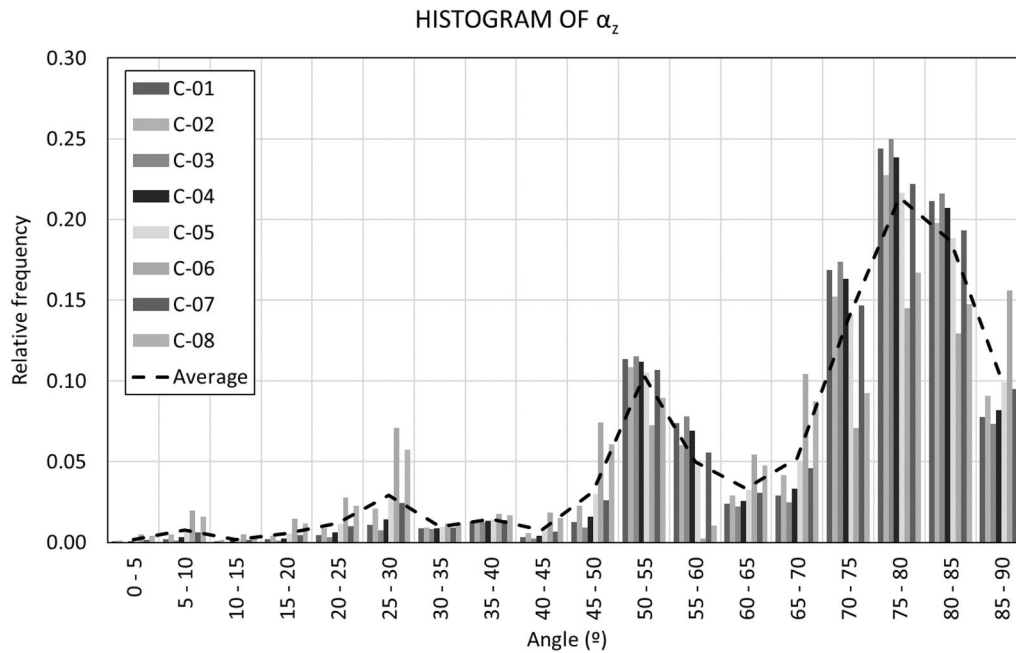


Fig. 11 Histogram of angle distribution with respect to the Z-axis

Table 2 Efficiency index

Prism	ei_x	ei_y	ei_z
C-01	0.602	0.588	0.313
C-02	0.571	0.597	0.328
C-03	0.612	0.585	0.307
C-04	0.591	0.591	0.318
C-05	0.550	0.602	0.339
C-06	0.417	0.641	0.407
C-07	0.561	0.600	0.334
C-08	0.459	0.628	0.386

In this research, it is assumed that the orientations of the fibers obtained from the miniprism are representative of the whole prism and, by extension, of the two cubes extracted from it. In this case, the data of interest is the efficiency index with respect to the axis perpendicular to the crack plane. In the case of top cubes, the efficiency index to be considered is ei_x , while in the case of side cubes, the efficiency index of interest is ei_z .

3.2 Pre-cracking Test

Table 3 shows the maximum vertical load P_{max} and the ultimate vertical load P_{ult} (i.e., the load when the test

Table 3 Results of the pre-cracking test

Specimen	Pre-crack loads			Fatigue loads	
	P_{max} (kN)	P_{ult} (kN)	P_{ult}/P_{max}	$P_{f,max}$ (kN)	$P_{f,min}$ (kN)
C-01-T	8.68	8.50	97.93%	7.38	0.43
C-01-S	6.30	6.17	97.94%	5.36	0.32
C-02-T	8.02	7.69	95.89%	6.82	0.40
C-02-S	5.23	5.03	96.18%	4.45	0.26
C-03-T	8.29	8.29	100.00%	7.05	0.41
C-03-S	7.31	6.64	90.83%	6.21	0.37
C-04-T	6.76	6.62	97.93%	5.75	0.34
C-04-S	7.92	7.78	98.23%	6.73	0.40
C-05-T	6.12	6.00	98.04%	5.20	0.31
C-05-S	6.86	6.73	98.10%	5.83	0.34
C-06-T	8.76	8.55	97.60%	7.45	0.44
C-06-S	6.68	6.42	96.11%	5.68	0.33
C-07-T	6.06	5.92	97.69%	5.15	0.30
C-07-S	6.55	6.32	96.49%	5.57	0.33
C-08-T	6.74	6.50	96.44%	5.73	0.34
C-08-S	7.26	6.99	96.28%	6.17	0.36

ends) obtained in the pre-cracking test for each of the specimen.

In the specimen identification code, C stands for "cube", the number represents the prism from which the cube is extracted and the letter at the end represents

the position of the groove. In this case, "T" stands for "top" while "S" stands for "side".

The results show that the cubes belonging to the T-position have a slightly higher maximum load than those belonging to the S-position. Specifically, the average value of the maximum load is 7.43 kN for the T-position and 6.76 kN for the S-position, which is approximately 9.8% more. When comparing the ultimate load values, the results show the same behavior, but more pronounced. In this case, the average value of the maximum load is 7.26 kN for the T-position and 6.52 kN for the S-position, which represents approximately 11.4% more. This shows that the S-position cubes, in which the fibers have an orientation substantially parallel to the notch and the crack, show a slightly less ductile behavior than the T-position cubes, in which the fibers have an orientation substantially perpendicular to the notch and the crack.

The fact that the cubes belonging to the T-position show a higher maximum load than those at position S denotes that the fibers cause an increase of the tensile strength of the concrete in their direction, which agrees with previous work performed by the authors (González et al., 2018a).

3.3 Fatigue Test

After the pre-cracking tests, all specimens were subjected to a cyclic load test up to specimen rupture. The maximum and minimum load values are given in Table 3. All the testing parameters have been described before. It is important to highlight two issues. First, given that the wedge splitting test can only apply tensile stresses to the specimen, the test performed is a tensile–tensile fatigue test. Second, this test does not evaluate the fatigue life of the concrete matrix in tension, but that of the reinforcement. That is, because during the first stage of the test, the concrete cracked and, therefore, does not directly contribute to the fatigue life. Then, there are two main mechanisms of the fibers that are capable of withstanding fatigue stresses: the tensile strength of the steel itself and the bonding forces of the fibers to the concrete matrix.

Commonly, fatigue tests are performed without pre-cracking. In this case, during the first part of the fatigue test, concrete bears the cyclic loads until it cracks. From this point on, fibers withstand the cyclic loads. In the case of fatigue test with pre-cracking (González et al., 2014, 2018b; Martinello et al., 2019; Vicente et al., 2019b), concrete matrix does not cooperate directly in supporting cyclic tension caused by the load cycles, because it is pre-cracked. The result is a smaller fatigue life. In any case, the concrete matrix indirectly cooperates in the fatigue response of the specimen by controlling the bonding capacity of the fibers and their degradation

mechanisms, and consequently, their ability to withstand cyclic loading.

Table 4 shows the fatigue life of each specimen. Fig. 12 shows the fatigue life results of the different specimens. Additionally, a Weibull fitting of the fatigue life results of the cubes belonging to the T-position on the one hand and those belonging to the S-position on the other hand has been performed. These curves are also shown in Fig. 12.

The results show how the cubes belonging to the T-position have a longer fatigue life than those belonging to the S-position. This value can be estimated to be approximately 5 times.

In the cubes belonging to the T-position, the fibers are better oriented (i.e., more clearly oriented in the direction of the tensile stresses), so they are more efficient. This results in a longer fatigue life. On the contrary, in the cubes belonging to the S-position, the fibers are mainly oriented in a direction perpendicular to the tensile stresses, so they are less efficient and, consequently, the fatigue life of the specimen is lower.

The fatigue behavior of the cubes can be further studied through the evolution of the crack opening with the loading cycles. The fatigue creep curves are the envelope of the maximum crack opening, which are shown in Fig. 13. Additionally, Fig. 14 shows the normalized fatigue creep curves, where abscissa is the damage "D", which is defined as the ratio between the number of cycle "n" and the fatigue life "N". Thus, all curves go from 0 to 1.

Fig. 13 shows how all the fatigue creep curves show very similar behavior. The curves can be divided into three parts. During the first part, there is a very rapid increase in crack opening. This increase gradually dampens until the second part is reached, where the growth is approximately linear. At the end, during the third part, a very rapid increase of the crack opening is observed again until the specimen breaks. This phenomenon has been widely observed in compressive fatigue tests (Medeiros et al., 2015; Ortega et al., 2022) and also in flexural fatigue

Table 4 Fatigue life

Specimen	N	Specimen	N
C-01-T	195,139	C-01-S	8,903
C-02-T	76,949	C-02-S	35,457
C-03-T	1,116,182	C-03-S	6,703
C-04-T	470,275	C-04-S	32,264
C-05-T	86,053	C-05-S	37,129
C-06-T	68,222	C-06-S	175,887
C-07-T	149,905	C-07-S	47,235
C-08-T	23,757	C-08-S	163,733

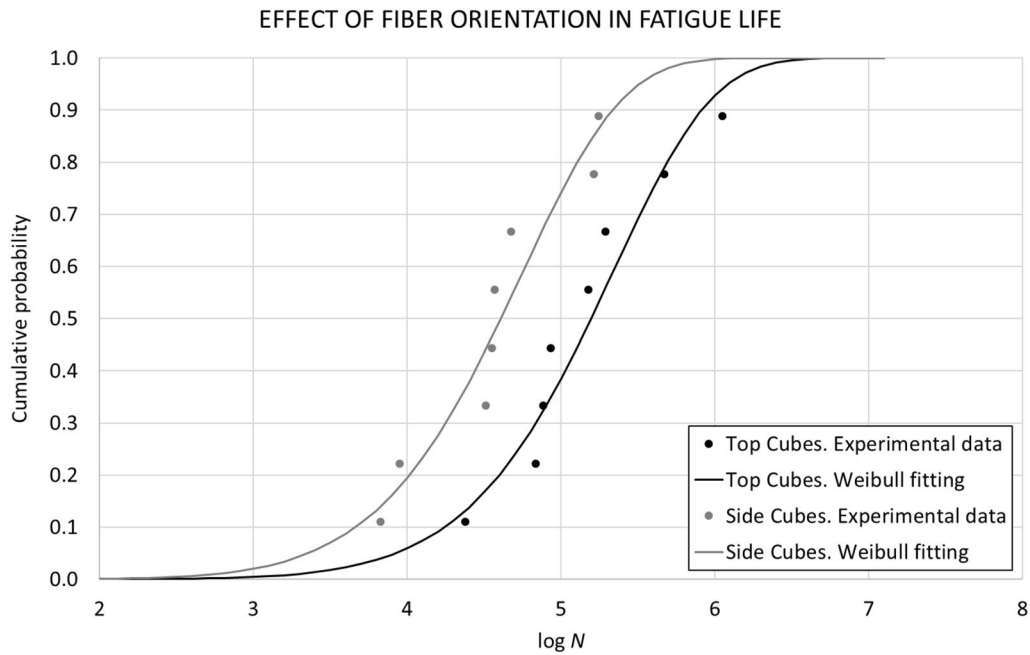


Fig. 12 Experimental fatigue life and Weibull fittings

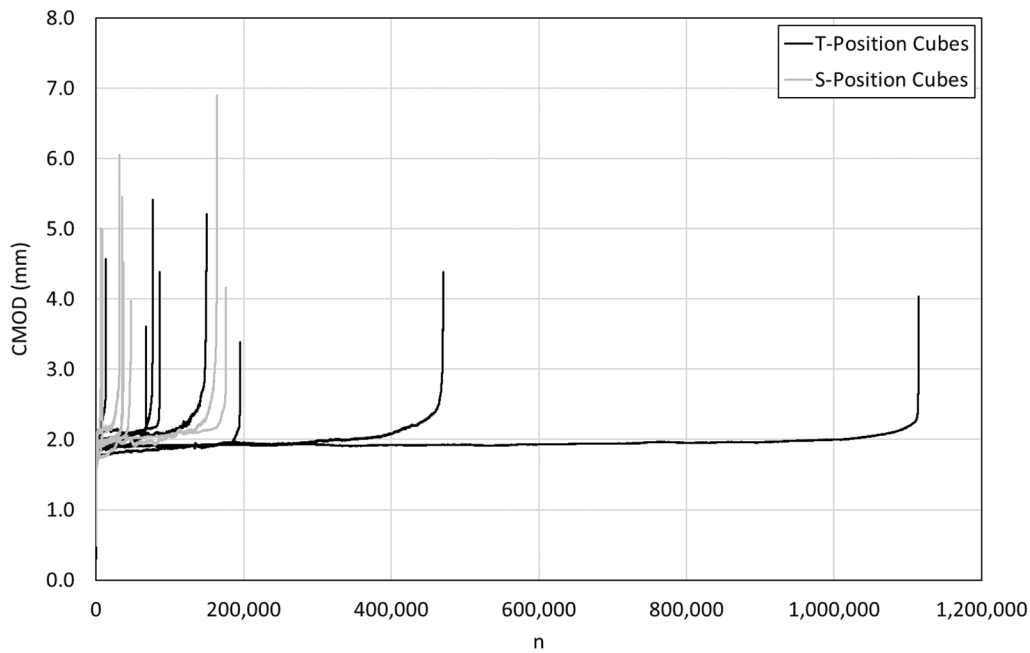


Fig. 13 Fatigue creep curves

tests (Martinello et al., 2019). The results obtained in this work (and shown in Fig. 14) demonstrate that this behavior also occurs in wedge splitting test where the CMOD is measured. This behavior is expected to be characteristic of concrete elements, regardless of the type of test

performed. In this case, the first part of the curve represents approximately the first 1% of the curve, while the third part represents approximately the 10% of the curve. These percentages are slightly different from those observed in the case of compressive fatigue. In particular,

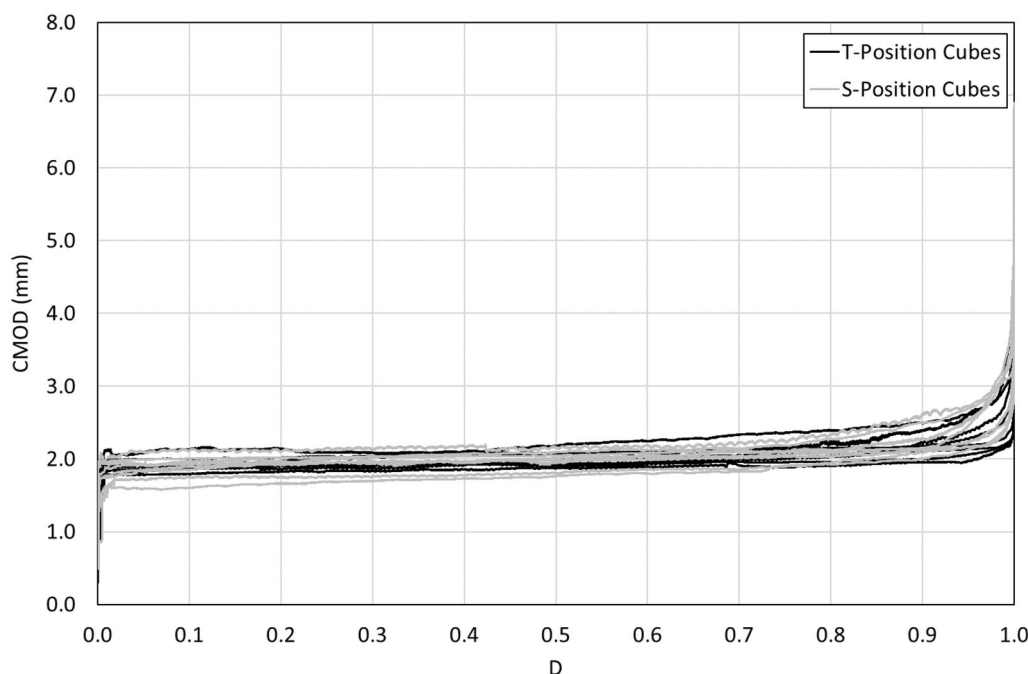


Fig. 14 Normalized fatigue creep curves

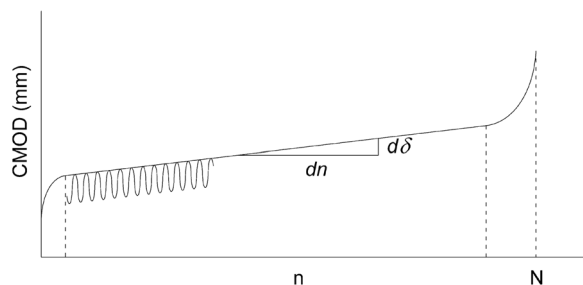


Fig. 15 Fatigue creep curve and crack opening rate per cycle

Table 5 Crack opening rate per cycle

Specimen	$d\delta/dn$	Specimen	$d\delta/dn$
C-01-T	9.02E-07	C-01-S	5.42E-05
C-02-T	3.89E-06	C-02-S	1.04E-05
C-03-T	7.54E-08	C-03-S	6.93E-05
C-04-T	4.38E-07	C-04-S	9.52E-06
C-05-T	2.46E-06	C-05-S	6.64E-06
C-06-T	4.41E-06	C-06-S	9.87E-07
C-07-T	2.11E-06	C-07-S	5.46E-06
C-08-T	1.38E-05	C-08-S	2.06E-06

the extension of the first part of the curve is very small in this case. This is because the tensile stress of the concrete matrix (until the crack appears) dominate this first part, and the specimens are already pre-cracked.

When the specimens are not pre-cracked, during the first part of the fatigue test, the cyclic loads are supported by the concrete matrix, micro-cracks are born and start growing and finally merge to create the visible crack. All this phenomenon is accompanied by a strong plastic deformation which is what forms the first part of the fatigue creep curve.

When the specimens are cracked, all this phenomenon has almost completely occurred during the pre-cracking process, so the first part of the curve is much smaller.

From the second part of the fatigue creep curve its slope, $d\delta/dn$, can be determined. By analogy with

compressive fatigue, this value is determined as *crack opening rate per cycle* (Fig. 15).

Table 5 shows the value of this parameter for all the specimens.

3.4 Correlation Between Fatigue Life and Crack Opening Rate Per Cycle

The crack opening rate per cycle has a linear relationship with the fatigue life N on a bi-logarithmic scale. This relationship was first shown in Sparks and Menzies (1973) for compressive fatigue testing and is commonly known as the Sparks–Menzies relationship. Fig. 16 shows the correlation between crack opening rate per cycle and fatigue life for all cubes, just with the linear fit to the data points.

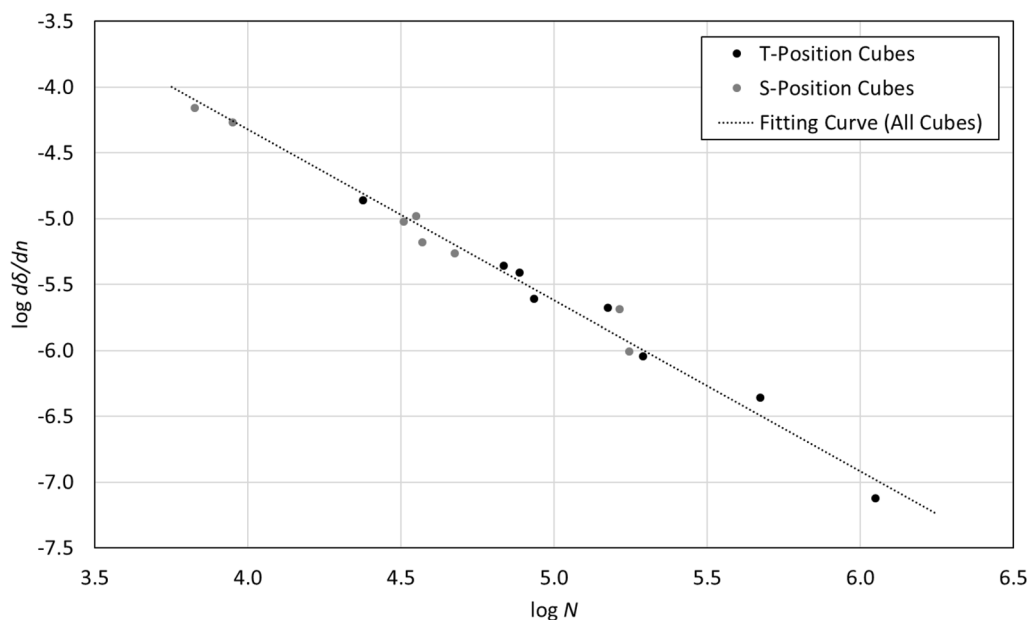


Fig. 16 Correlation between the crack opening rate per cycle and the fatigue life

As can be seen in Fig. 16, the results of all the cubes together show a good correlation (coefficient $R^2=0.98$), which reveals that the relationship between crack opening rate per cycle and fatigue life is independent of the fibers; it only depends on the concrete matrix. The specimens with the best oriented fibers (T-Position Cubes) show a higher fatigue life and a smaller value of the crack opening rate per cycle, i.e., these specimens are located in the lower right half of the graph. In contrast, the specimens with the worst oriented fibers (S-Position Cubes) show a shorter fatigue life and a higher value of the crack opening rate per cycle, i.e., these specimens are located in the upper left half of the graph.

3.5 Correlation Between Fatigue Life and Efficiency Index

Fatigue life is related to fiber content and fiber orientation, as the fibers help to withstand the cyclic loads and, therefore, the more fibers and/or the better the fiber orientation, the longer the fatigue life.

In this particular case, all the cubes have approximately the same fiber content, but the orientation of the fibers is significantly different between the cubes belonging to the T series and the cubes belonging to the S series (this is an advantage of this test compared to the conventional three-point bending test). As explained above, fibers are approximately oriented in the horizontal plane of the prism, which means that they are oriented sensibly perpendicular to the crack in the case of the specimens belonging to the T series, and they are oriented sensibly parallel to the crack in the case of the specimens

belonging to the S series. Fig. 17 shows the relationship between the fatigue life and the efficiency index (ei_x for T series specimens and ei_z for S series specimens).

The results show that there is a correlation between both parameters, such that the higher the efficiency index, the longer the fatigue life. This conclusion can also be drawn from Tables 2 and 4. These tables, analyzed together, show that the T series has higher fatigue life values and higher efficiency index, while the S series has lower fatigue life values and lower efficiency index.

However, the correlation is not so strong than one might think a priori (coefficient $R^2=0.58$). This is because the efficiency indices have been obtained, for each prism, from its corresponding miniprism (see Fig. 2) and have been considered the entire miniprism.

At this point, when Fig. 5 is observed in detail, it can be detected that the fibers are clearly oriented in the XY plane, especially in the lower and upper parts of the concrete prism (and, therefore, also in the miniprism), which are two of the regions affected by the "wall effect". However, in the central part of the miniprism, the percentage of fibers with a more vertical orientation is higher. If a local analysis is carried out, focused only on the fibers that pass through the cracks during the test, it can be observed that the fiber orientation is slightly different. In the case of cubes belonging to the T series, the fibers that govern the fatigue response are those located in the lower half of the cube, with those located in the part closest to the middle plane of the cube being more relevant. In the case of the cubes

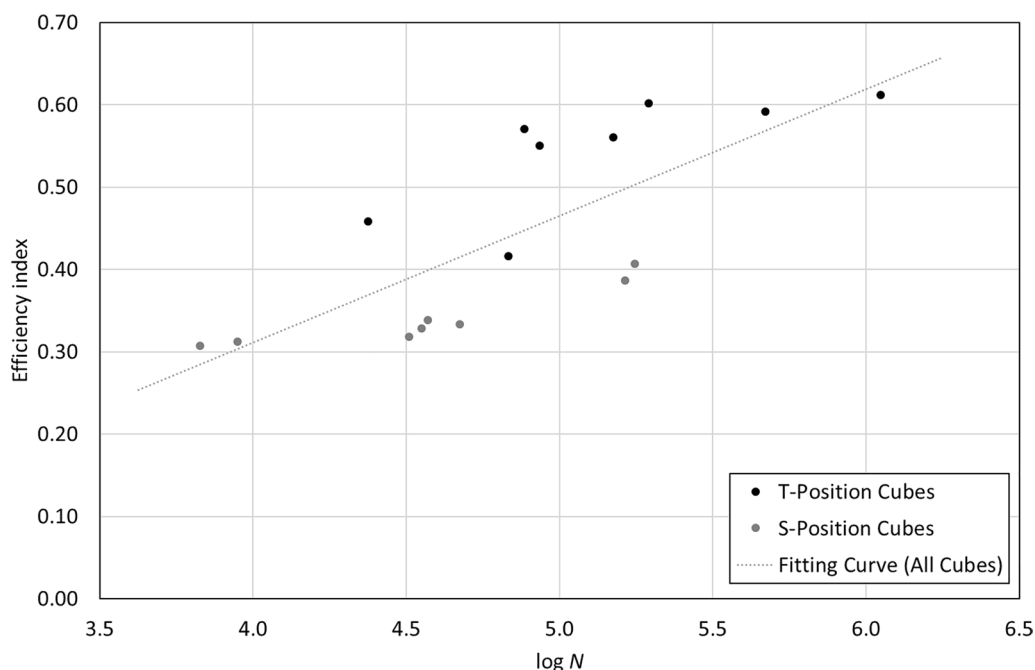


Fig. 17 Correlation between the fatigue life and the efficiency index

Table 6 Efficiency index of the central third

Prism	ei_x	ei_z
C-01	0.552	0.363
C-02	0.493	0.406
C-03	0.612	0.307
C-04	0.591	0.318
C-05	0.465	0.424
C-06	0.383	0.441
C-07	0.507	0.387
C-08	0.366	0.479

belonging S series specimens, the fibers that govern the fatigue response are those located in the middle plane of the cube. Extrapolating this reasoning to the concrete prism (or miniprism), it is concluded that the fibers located in the central region of the prism have the greatest influence on the fatigue response of the cubes.

Table 6 shows the efficiency indexes ei_x and ei_z for all the prisms particularized for the central third.

Fig. 18 shows the relationship between the fatigue life and the efficiency index of the central third (ei_x for T series specimens and ei_z for S series specimens).

In this case, the correlation is now strong ($R^2 = 0.82$).

3.6 Correlation Between Crack Opening Rate Per Cycle and Efficiency Index

Fig. 19 shows the relationship between the crack opening rate per cycle and the efficiency index.

Again, there is a relationship between the two parameters, so that the higher the efficiency index, the lower the crack opening rate per cycle. This means that the better the fiber orientation, the smaller the crack growth per cycle.

As in the previous case, the relationship between the two parameters is not very strong (coefficient $R^2 = 0.57$). The explanation is the same as the one described above; the efficiency index used in the comparisons is the one obtained from the miniprism, implicitly assuming that it is the same throughout the prism (and, therefore, also in the two cubes coming out of it). However, when considering the fibers that cross the crack, which in this case corresponds approximately to the fibers located in the central third of the miniprism, the correlation improves substantially.

Fig. 20 shows the relationship between the crack opening rate per cycle and the efficiency index of the central third.

Again, the correlation improves substantially ($R^2 = 0.80$).

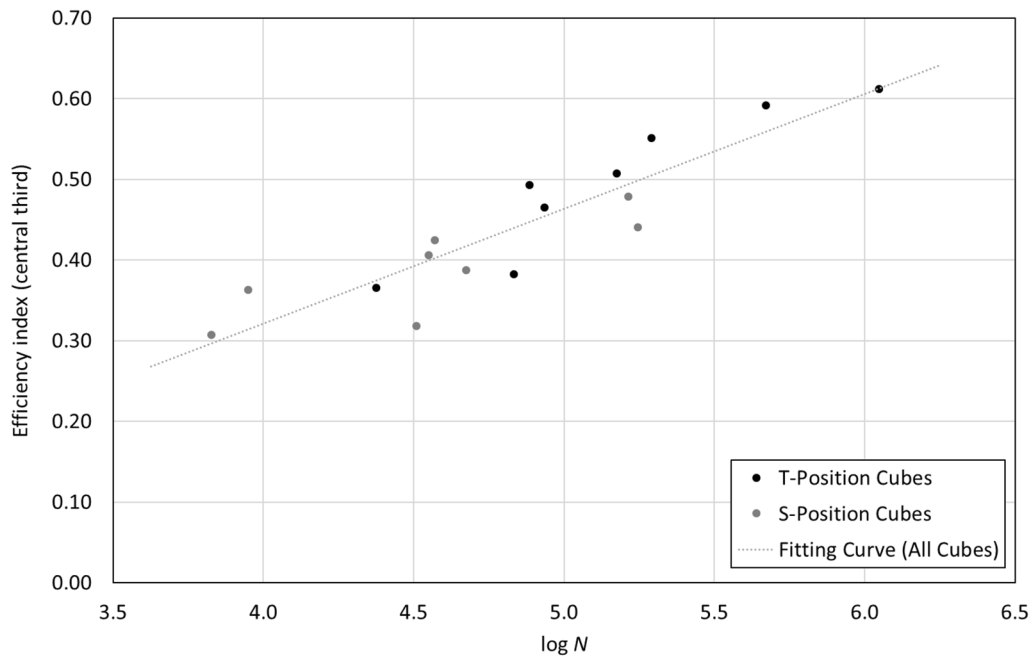


Fig. 18 Correlation between the fatigue life and the efficiency index of the central third

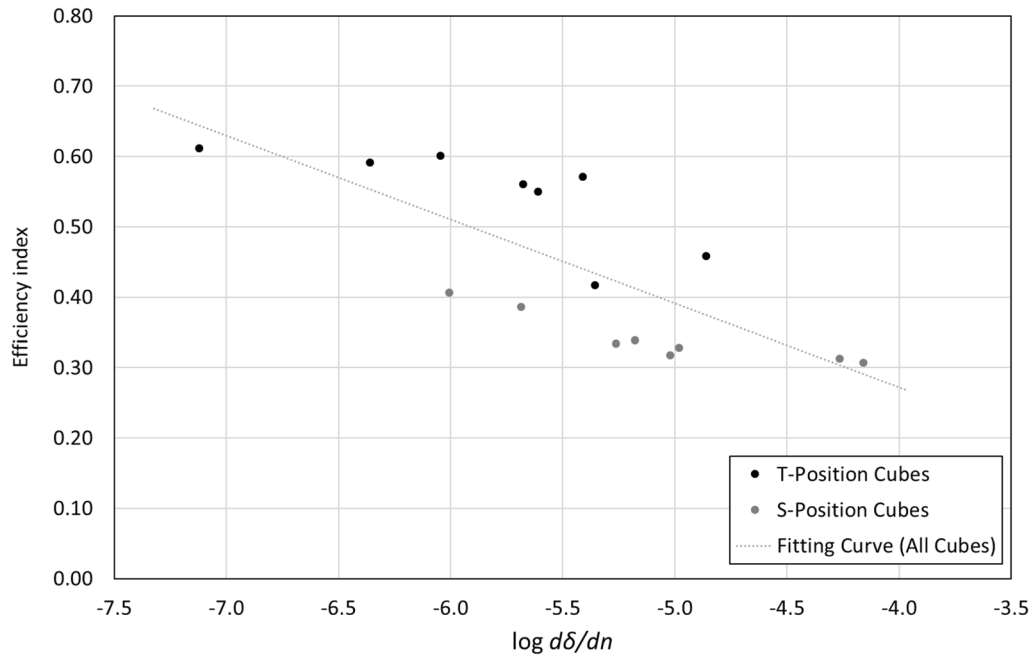


Fig. 19 Correlation between the crack opening rate per cycle and the efficiency index

4 Conclusions

In this research work, the influence of fiber orientation on the fatigue response of steel fiber-reinforced concrete is analyzed. The evaluation of the fiber

arrangement has been carried out by combining micro-CT scanning and post-processing with image analysis software. As for the fatigue response, wedge splitting tests (WST) were performed. The concrete mix produced had a fiber content of 2% by volume.

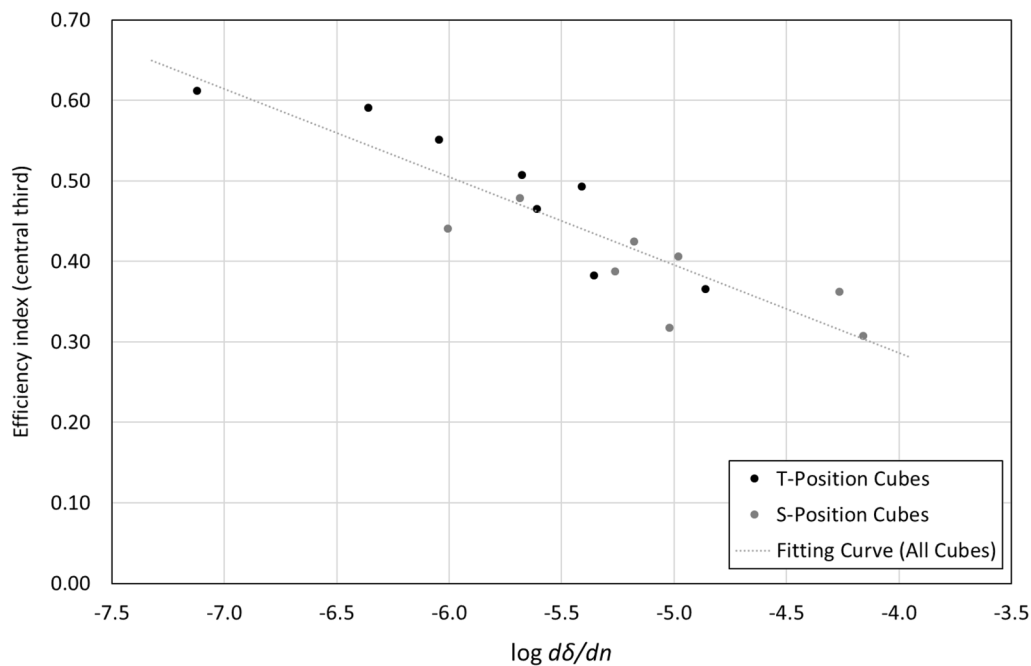


Fig. 20 Correlation between the crack opening rate per cycle and the efficiency index of the central third

A total of 8 standard prisms of $150 \times 150 \times 600$ mm were fabricated. Then, from each prism, 2 cubes of 150 mm edge and a miniprism of $50 \times 50 \times 150$ mm were cut. The cubes were next grooved and notched. In one cube per prism, the groove and notch were made on its top face, while in the other cube, they were made on its side face. In this way, it is ensured that the preferred orientation of the fibers (with respect to the crack surface) in each cube is significantly different. In any case, the actual fiber orientation of each prism was obtained with a micro-CT scanner.

Based on the findings of the experimental program presented in this paper, the following conclusions can be drawn:

1. Micro-CT reveals that the fibers tend to be positioned in the horizontal plane, i.e., perpendicular to the Z-axis, the one corresponding to the direction of concrete pouring. In the XY plane, no clear orientation tendency is observed. Next, the efficiency index is obtained for each prism and each direction (X, Y and Z). In all cases, the relevant efficiency index is the one belonging to the axis perpendicular to the cracking surface of the cubes. In the case of the T-position cubes, the efficiency index along the X-axis governs their mechanical behavior, while in the case of the S-position cubes, it is the efficiency index along the Z-axis that does so.
2. Pre-cracking static tests reveal that the T-position cubes have a slightly higher maximum load and ultimate load than the S-position cubes. This finding shows that the T-position cubes, whose fibers are better oriented, have a higher mechanical capacity.
3. Fatigue tests show that the T series cubes have, in general, a longer fatigue life than the S series cubes. On the other hand, the analysis of the fatigue creep curve reveals that the first stage of the diagram is very small (only 1% of the total). This particularly low value, compared to other fatigue tests, is explained by the fact that the specimens are pre-cracked. On the contrary, the crack opening rate per cycle shows smaller values for the T series cubes than for the S series.
4. When the fatigue life is plotted against the crack opening rate per cycle (both parameters in logarithmic scale), a strong linear relationship between them is observed. In this case, all the tests of both series are aligned, which shows that this correlation (Sparks and Menzies' Law) does not depend on the fiber orientation, but only on the concrete matrix.
5. If the fiber efficiency indexes are compared with the fatigue parameters (fatigue life and crack opening rate per cycle), it is found that there is a clear relationship between them. The relationship is not very strong when considering the efficiency indexes over the entire volume of the miniprism. However, when

the efficiency indexes of the central third of the mini-prism (which has been assumed to be similar to that of the fibers crossing the cracks) are considered, the relationship is much more robust.

Acknowledgements

The authors are grateful for the financial support from the Ministerio de Ciencia e Innovación, PID2019-110928RB-C32, Spain.

Author contributions

Gonzalez D.C. made a contribution to conception and design of the research, supervise the test results and write the manuscript. Mena-Alonso A. made a contribution to conduct the experimental test, carry out the laboratory work and analysis of the test results, Minguez J. made a contribution in the conceptual design of the test, Martínez J.A. made a contribution to conduct the experimental test and revise the manuscript. Vicente M.A. made a contribution to conception and design of the research and revise the manuscript. All authors read and approved the final manuscript.

Funding

This investigation was supported by the following funder: Ministerio de Ciencia e Innovación, PID2019-110928RB-C32, Spain.

Availability of data and materials

All data generated or analyzed during this study are included in this published paper.

Declarations

Ethics approval and consent to participate

Not applicable.

Consent for publication

Not applicable.

Competing interests

No competing interests exist in the submission of this manuscript, and manuscript is approved by all authors for publication. The authors declare that the work described was original research that has not been published previously, and not under consideration for publication elsewhere, in whole or in part.

Received: 7 April 2023 Accepted: 26 August 2023

Published online: 12 January 2024

References

- Ahmand, J., & Zhou, Z. (2022). Mechanical properties of natural as well as synthetic fiber reinforced concrete: A review. *Construction and Building Materials*, 333, 127353.
- Akgol, O., Unal, E., Bağmancı, M., Karaaslan, M., Sevim, U. K., Öztürk, M., & Bhardauria, A. (2019). A nondestructive method for determining fiber content and fiber ratio in concretes using a metamaterial sensor based on a v-shaped resonator. *Journal of Electronic Materials*, 48, 2469–2481.
- Ali, B., Qureshi, L. A., & Khan, S. U. (2020a). Flexural behavior of glass fiber-reinforced recycled aggregate concrete and its impact on the cost and carbon footprint of concrete pavement. *Construction and Building Materials*, 262, 120820.
- Ali, B., Qureshi, L. A., & Kurda, R. (2020b). Environmental and economic benefits of steel, glass, and polypropylene fiber reinforced cement composite application in jointed plain. *Composite Communications*, 22, 100437.
- Al-Mattarneh, H. (2014). Electromagnetic quality control of steel fiber concrete. *Construction and Building Materials*, 73, 350–356.
- American Society for Testing and Materials. (2019). *ASTM C1609/C1609M-12. Standard test method for flexural performance of fiber-reinforced concrete (Using beam with third-point loading)*. American Society for Testing and Materials.
- Balazs, G. L., Czoboly, O., Lubloy, E., Kapitany, K., & Barsi, A. (2017). Observation of steel fibers in concrete with computed tomography. *Construct. Build. Mater.*, 140(2017), 534–541.
- Batrukin, D., Hisseine, O. A., Masmoudi, R., & Tagnit-Hamou, A. (2021). Valorization of recycled FRP materials from wind turbine blades in concrete. *Resources, Conservation & Recycling*, 174, 105807.
- British Standards Institution. (2008). *EN 14651:2005+A1:2007 (2008). Test method for metallic fibre concrete. Measuring the flexural tensile strength (limit of proportionality (LOP), residual)*. British Standards Institution.
- British Standards Institution. (2016). *EN 196-1:2016. Methods of testing cement. Determination of strength*. British Standards Institution.
- Brühwiler, E., & Wittmann, F. H. (1990). The wedge splitting test, a new method of performing stable fracture mechanics tests. *Engineering Fracture Mechanics*, 35(1/2/3), 117–125.
- Cachim, P. B., Figueiras, J. A., & Pereira, P. A. A. (2002). Fatigue behavior of fiber-reinforced concrete in compression. *Cement & Concrete Composites*, 24, 211–217.
- Conforti, A., Cuenca, E., Zerbino, R., & Plizzari, G. A. (2021). Influence of fiber orientation on the behavior of fiber reinforced concrete slabs. *Structural Concrete*, 22, 1831–1844.
- Cui, K., Xu, L., Li, L., & Chi, Y. (2023). Mechanical performance of steel-polypropylene hybrid fiber reinforced concrete subject to uniaxial constant-amplitude cyclic compression: Fatigue behavior and unified fatigue equation. *Composite Structures*, 311, 116795.
- Cui, K., Xu, L., Li, X., Hu, X., Huang, L., Deng, F., & Chi, Y. (2021). Fatigue life analysis of polypropylene fiber reinforced concrete under axial constant-amplitude cyclic compression. *Journal of Cleaner Production*, 319, 128610.
- Deng, F., Chi, Y., Xu, L., Huang, L., & Hu, X. (2021). Constitutive behavior of hybrid fiber reinforced concrete subject to uniaxial cyclic tension: Experimental study and analytical modeling. *Construction and Building Materials*, 295, 123650.
- Forsat, M., Mirjavadi, S. S., & Hamouda, A. M. S. (2019). Investigation of the effect of Larestan's pipeline water on the mechanical properties of concretes containing granite aggregates. *Advances in Civil Engineering*. <https://doi.org/10.1155/2019/4197186>
- Gao, D., Gu, Z., Wei, C., Wu, C., & Pang, Y. (2021). Effects of fiber clustering on fatigue behavior of steel fiber reinforced concrete beams. *Construction and Building Materials*, 301, 124070.
- González, D. C., Minguez, J., Vicente, M. A., Cambroner, F., & Aragón, G. (2018a). Study of the effect of the fibers' orientation on the post-cracking behavior of steel fiber reinforced concrete from wedge-splitting tests and computed tomography scanning. *Construction and Building Materials*, 192, 110–122.
- González, D. C., Moradillo, R., Minguez, J., Martínez, J. A., & Vicente, M. A. (2018b). Postcracking residual strengths of fiber-reinforced high-performance concrete after cyclic loading. *Structural Concrete*, 19, 340–351.
- González, D. C., Rahman, M., Minguez, J., Vicente, M. A., & Hindi, R. (2020). Influence of fibers and curing conditions on the pore morphology in plain and fiber-reinforced high-performance concrete through the use of computed tomography scan technology. *Applied Sciences*, 10(12), 4286.
- González, D. C., Vicente, M. A., & Ahmad, S. (2014). Effect of cyclic loading on the residual tensile strength of steel fiber-reinforced high-strength concrete. *Journal of Materials in Civil Engineering*, 27(9), 04014241.
- Herrmann, H., Pastorelli, E., Kallonen, A., & Suuronen, J. P. (2016). Methods for fibre orientation analysis of X-ray tomography images of steel fibre reinforced concrete (SFRC). *Journal of Materials Science*, 51(8), 3772–3783.
- Isojeh, B., El-Zeghayar, M., & Vecchio, F. J. (2017). Fatigue behavior of steel fiber concrete in direct tension. *Journal of Materials in Civil Engineering*, 29(9), 01017130.
- Khan, M., Cao, M., Xie, C., & Ali, M. (2022). Effectiveness of hybrid steel-basalt fiber reinforced concrete under compression. *Case Studies in Construction Materials*, 16, e00941.
- Khan, M., Rehman, A., & Ali, M. (2020). Efficiency of silica-fume content in plain and natural fiber reinforced concrete for concrete road. *Construction and Building Materials*, 244, 118382.
- Laranjeira, F., Grünwald, S., Walraven, J., Blom, C., Molins, C., & Aguado, A. (2011). Characterization of the orientation profile of steel fiber reinforced concrete. *Materials and Structures*, 44, 1093–1111.

- Lee, J.-H. (2017). Influence of concrete strength combined with fiber content in the residual flexural strengths of fiber reinforced concrete. *Composite Structures*, *168*, 216–225.
- Li, L., Xia, J., Chin, C., & Jones, S. (2020). Fibre distribution characterization of ultra-high performance fibre-reinforced concrete (UHPFRC) plates using magnetic probes. *Materials (basel)*, *13*, 5064.
- Linsbauer, H. N., & Tschegg, E. K. (1986). Fracture energy determination of concrete with cube-shaped specimens. *Zement Und Beton*, *31*, 38–40. In German.
- Martinello, D., De la Fuente, A., & Pialariss, S. H. (2019). Fatigue of cracked high performance fiber reinforced concrete subjected to bending. *Construction and Building Materials*, *220*, 444–455.
- Medeiros, A., Zhang, X., Ruiz, G., Yu, R. C., & De Souza, M. (2015). Effect of the loading frequency on the compressive fatigue behavior of plain and fiber reinforced concrete. *International Journal of Fatigue*, *70*, 342–350.
- Mehdipour, I., Horst, M., Zoughi, R., & Khayat, K. H. (2017). Use of near-field microwave reflectometry to evaluate steel fiber distribution in cement-based mortars. *Journal of Materials in Civil Engineering*, *29*, 1–12.
- Mena, A., González, D. C., Mínguez, J., & Vicente, M. A. (2020). Computed tomography beyond medicine: Applications to the microstructural study of concrete and other engineering materials. *Hormigón y Acero*, *71*(292), 7–19.
- Mínguez, J., González, D. C., & Vicente, M. A. (2018). Fiber geometrical parameters of fiber-reinforced high strength concrete and their influence on the residual post-peak flexural tensile strength. *Construction and Building Materials*, *168*, 906–922.
- Mínguez, J., Gutiérrez, L., González, D. C., & Vicente, M. A. (2019). Plain and fiber-reinforced concrete subjected to cyclic compressive loading: study of the mechanical response and correlations with microstructure using CT scanning. *Applied Sciences*, *9*(15), 3030.
- Mobasher, B., Bakhshi, M., & Barsby, C. (2014). Back calculation of residual tensile strength of regular and high performance fiber reinforced concrete from flexural tests. *Construction and Building Materials*, *70*, 243–253.
- Mudadu, A., Tiberti, G., Germano, F., Pizzari, G. A., & Morbi, A. (2018). The effect of fiber orientation on the post-cracking behavior of steel fiber reinforced concrete under bending and uniaxial tensile tests. *Cement and Concrete Composites*, *93*, 274–288.
- Nilforoush, R., Milsson, M., & Elfgren, L. (2017). Experimental evaluation of tensile behavior of single cast-in-place anchor bolts in plain and steel fibre reinforced normal- and high-strength concrete. *Engineering Structures*, *147*, 195–206.
- Nogueira, V., Taissum, D. C., & De Andrade, F. (2021). Creep mechanisms in precracked polypropylene and steel fiber-reinforced concrete. *Journal of Materials in Civil Engineering*, *33*(8), 04021187.
- Oesch, T., Landis, E., & Kuchma, D. (2018). A methodology for quantifying the impact of casting procedure on anisotropy in fiber-reinforced concrete using X-ray CT. *Materials and Structures*, *51*, 73. <https://doi.org/10.1617/s11527-018-1198-8>
- Ortega, J. J., Ruiz, G., Poveda, E., González, D. C., Tarifa, M., Zhang, X. X., Yu, R. C., Vicente, M. A., De la Rosa, A., & Garijo, L. (2022). Size effect on the compressive fatigue of fibre-reinforced concrete. *Construction and Building Materials*, *322*, 126238.
- Ozturk, O., & Ozyurt, N. (2022). Sustainability and cost-effectiveness of steel and polypropylene fiber reinforced concrete pavement mixtures. *Journal of Cleaner Production*, *363*, 132582.
- Pastorelli, E.; Herrmann, H. (2016). "Time-efficient automated analysis for fibre orientations in steel fibre reinforced concrete". Proceedings of the Estonian Academy of Sciences, pp. 28–36.
- Ponikiewski, T., & Katzer, J. (2016). X-ray computed tomography of fibre reinforced self-compacting concrete as a tool of assessing its flexural behavior. *Materials and Structures*, *49*, 2131–2140.
- Riedel, P., & Leutbecher, T. (2021). Effect of fiber orientation on compressive strength of ultra-high-performance fiber-reinforced concrete. *ACI Materials Journal*, *118*(2), 199–209.
- Ríos, J. D., Mínguez, J., & Martínez – De la Concha, A., Vicente, M.A., Cifuentes, H. (2020). Microstructural analyses of the addition of PP fibres on the fracture properties of high-strength self-compacting concrete by X-ray computed tomography. *Construction and Building Materials*, *261*, 120499.
- Ruan, T., & Poursaee, A. (2019). Fiber-distribution assessment in steel fiber-reinforced UHPC using conventional imaging, X-Ray CT scan, and concrete electrical conductivity. *Journal of Materials in Civil Engineering*, *31*(8), 04019133.
- Saradar, A., Tahmouresi, B., Mohseni, E., & Shadmani, A. (2018). Restrained shrinkage cracking of fiber-reinforced high-strength concrete. *Fibers*. <https://doi.org/10.3390/fib6010012>
- Shah, I., Li, J., Yang, S., Zhang, Y., & Anwar, A. (2022). Experimental investigation on the mechanical properties of natural fiber reinforced concrete. *Journal of Renewable Materials*, *10*(5), 1307–1320.
- Shahrabadi, H., Nikoo, H. S., & Forsat, M. (2017). Effect of limestone on the mechanical properties of concrete containing silica fume and fly ash. *Journal of Materials and Environmental Sciences*, *8*(2), 457–466.
- Shen, D., Liu, C., Kang, J., Yang, Q., Li, M., & Li, C. (2022). Early-age autogenous shrinkage and tensile creep of hooked-end steel fiber reinforced concrete with different thermal treatment temperatures. *Cement and Concrete Composites*, *131*, 104550.
- Sparks, P. R., & Menzies, J. B. (1973). Effect of rate of loading upon static and fatigue strengths of plain concrete in compression. *Magazine of Concrete Research*, *25*(83), 73–80.
- Vicente, M. A., González, D. C., & Mínguez, J. (2014). Determination of dominant fibre orientations in fibre-reinforced high strength concrete elements based on computed tomography scans. *Nondestructive Testing and Evaluation*, *29*(2), 164–182.
- Vicente, M. A., González, D. C., & Mínguez, J. (2019). Recent advances in the use of computed tomography in concrete technology and other engineering fields. *Micron*, *118*, 22–34.
- Vicente, M. A., Mena, A., Mínguez, J., & González, D. C. (2021). Use of computed tomography scan technology to explore the porosity of concrete: Scientific possibilities and technological limitations. *Applied Sciences*, *11*(18), 8699.
- Vicente, M.A.; Mínguez, J.; González, D.C. (2017). The use of computed tomography to explore the microstructure of materials in civil engineering: from rocks to concrete, in: Halefoglu Ahmet Mesur (Ed.), Computed tomography—advanced applications, InTech.
- Vicente, M. A., Mínguez, J., & González, D. C. (2019). Computed tomography scanning of the internal microstructure, crack mechanisms, and structural behavior of fiber-reinforced concrete under static and cyclic bending tests. *International Journal of Fatigue*, *121*, 9–19.
- Vicente, M. A., Ruiz, G., González, D. C., Mínguez, J., Tarifa, M., & Zhang, X. (2018). CT-Scan study of crack patterns of fiber-reinforced concrete loaded monotonically and under low-cycle fatigue. *International Journal of Fatigue*, *114*, 138–147.
- Vicente, M. A., Ruiz, G., González, D. C., Mínguez, J., Tarifa, M., & Zhang, X. (2019). Effects of fiber orientation and content on the static and fatigue behavior of SFRC by using CT-Scan technology. *International Journal of Fatigue*, *128*, 105178.
- Vrijdaghs, R., Di Prisco, M., & Vandewalle, L. (2018). Uniaxial tensile creep of a cracked polypropylene fiber reinforced concrete. *Materials and Structures*. <https://doi.org/10.1617/s11527-017-1132-5>
- Yazdanbakhsh, A., Bank, L. C., Rieder, K.-A., Tian, Y., & Chen, C. (2018). Concrete with discrete slender elements from mechanically recycled wind turbine blades. *Resources, Conservation & Recycling*, *128*, 11–21.
- Yoo, D. Y., & Yoon, Y. S. (2015). Structural performance of ultra-high-performance concrete beams with different steel fibers. *Engineering Structures*, *102*, 409–423.
- Yuan, Z., & Jian, Y. (2021). Mechanical properties and microstructure of glass fiber and polypropylene fiber reinforced concrete: An experimental study. *Construction and Building Materials*, *266*, 121048.
- Zhou, B., & Uchida, Y. (2017). Relationship between fiber orientation/distribution and post-cracking behavior in ultra-high-performance fiber-reinforced concrete (UHPFRC). *Cement and Concrete Composites*, *83*, 66–75.
- Zia, A., & Ali, M. (2017). Behavior of fiber reinforced concrete for controlling the rate of cracking in canal-lining. *Construction and Building Materials*, *155*, 726–739.

Publisher's Note

Springer Nature remains neutral with regard to jurisdictional claims in published maps and institutional affiliations.

Dorys C. González Associate Professor, E. Politécnica Superior, Universidad de Burgos, Campus Milanera (Edif. D), c/Villadiego s/n, 09001

Burgos, Spain.

Álvaro Mena-Alonso Postdoctoral Researcher, E. Politécnica Superior, Universidad de Burgos, Campus Milanera (Edif. D), c/Villadiego s/n, 09001 Burgos, Spain.

Jesús Mínguez Associate Professor, E. Politécnica Superior, Universidad de Burgos, Campus Milanera (Edif. D), c/Villadiego s/n, 09001 Burgos, Spain.

José A. Martínez Associate Professor, E. Politécnica Superior, Universidad de Burgos, Campus Milanera (Edif. D), c/Villadiego s/n, 09001 Burgos, Spain.

Miguel A. Vicente Associate Professor, E. Politécnica Superior, Universidad de Burgos, Campus Milanera (Edif. D), c/Villadiego s/n, 09001 Burgos, Spain.

Submit your manuscript to a SpringerOpen[®] journal and benefit from:

- ▶ Convenient online submission
- ▶ Rigorous peer review
- ▶ Open access: articles freely available online
- ▶ High visibility within the field
- ▶ Retaining the copyright to your article

Submit your next manuscript at ▶ [springeropen.com](https://www.springeropen.com)
